Title

A STUDY OF DIFFUSION PHENOMENA IN THE BARE EARTH REGION: THE REACTION 159Tb + 620 MeV 86Kr

Author

Wozniak, G.J.

Publication Date

1977-09-01

Submitted to Nuclear Physics A

LBL-6532
Preprint

A STUDY OF DIFFUSION PHENOMENA IN THE RARE EARTH REGION: THE REACTION ^{159}Tb + 620 MeV ^{86}Kr

G. J. Wozniak, R. P. Schmitt, P. Glässel, and
L. G. Moretto

September 1977

Prepared for the U. S. Energy Research and
Development Administration under Contract W-7405-ENG-48

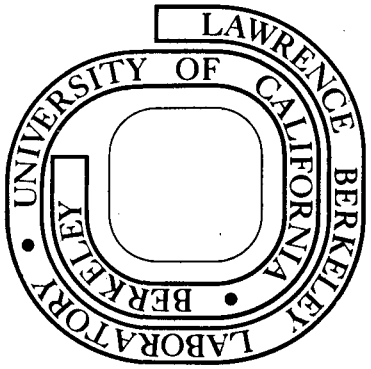

DISCLAIMER

A STUDY OF DIFFUSION PHENOMENA IN THE RARE EARTH REGION: THE REACTION ^{159}Tb + 620 MeV ^{86}Kr*

G. J. Wozniak, R. P. Schmitt, P. Glässel[+] and L. G. Moretto[++]
Department of Chemistry and
Lawrence Berkeley Laboratory
University of California
Berkeley, California 94720

ABSTRACT

Kinetic energy spectra, charge and angular distributions have been measured with ΔE-E telescopes for over 25 identified elements from the reaction ^{159}Tb + 620 MeV ^{86}Kr. At all angles and for all observed atomic numbers, the energy spectra indicate the presence of energetically relaxed products in the vicinity of the Coulomb barrier. Elements near the projectile also show a sizable contribution from incompletely damped events at angles close to the grazing angle. The charge distributions are peaked near the projectile Z and demonstrate a strong shape dependence on the angle of observation. The angular distributions show a weakening of the side peaking with increasing proton transfer to or from the projectile. Angular distributions and angle-integrated charge distributions have been calculated with a diffusion model which assumes the formation of a rotating intermediate complex with an ℓ-dependent lifetime. The mass exchange between the two segments of the intermediate complex is treated as a diffusive process which is described by the Master Equation. Values for the diffusion constant, the overlap of the two density distributions, the mean lifetime of the intermediate complex and the spread in the average lifetime were used which semi-quantitatively reproduced data from the 620 MeV ^{86}Kr reaction on

^{181}Ta and ^{197}Au targets. Satisfactory agreement was obtained between these calculations and the data from the ^{159}Tb target. In addition, by increasing the lifetime of the complex by 30%, the previously measured data for the $^{107,109}Ag$ + 620 MeV ^{86}Kr reaction was semi-quantitatively reproduced.

*This work was done with support from the U.S. Energy Research and Development Administration.
+Present address: Physikalisches Institut der Universität Heidelberg Philosophenweg 12, D-69, Heidlelberg, W. Germany
++Sloan Fellow 1974-76 Extended support.

E NUCLEAR REACTIONS $^{159}Tb(^{86}Kr,Z)$, E_{lab} = 620 MeV; measured $\sigma(E,Z,\theta)$, for $20 \leqslant Z \leqslant 48$; deduced: charge diffusion constants and ℓ-dependent lifetime of intermediate complex for $^{107,109}Ag$ and ^{159}Tb + 620 MeV ^{86}Kr.

1. Introduction

With the advent of heavy ion accelerators, many new physical phenomena have revealed themselves in heavy ion reactions studies[1-10]). In particular, studies with Kr beams gave evidence for phenomena which were characterized by a large energy dissipation and a relatively small amount of mass transfer[10-12]). Recent detailed studies[13-16]) of the systems ^{197}Au, ^{181}Ta and ^{107,109}Ag + 620 MeV ^{86}Kr have demonstrated evidence for diffusive relaxation along the mass asymmetry coordinate.

Substantial evidence of relaxation mechanisms has been observed in connection with a number of collective degrees of freedom[3,4]) in deep inelastic collisions. The experimental evidence suggests a hierarchy[3]) of characteristic times in the relaxation modes. From faster to slower, one can list the neutron-to-proton ratio of the fragments, their relative motion, the fragment intrinsic rotation and the mass asymmetry of the system. The relaxation of the mass asymmetry mode extends well into times when all of the previous modes have essentially reached equilibrium.

It is useful to think of the deep inelastic collision mechanism as involving a reaction intermediate or intermediate complex[17,18]) which, during its lifetime, undergoes equilibration processes which are interrupted at various stages of completion at the time of decay. The dissipation of large amounts of kinetic energy into internal degrees of freedom generates a thermal background which introduces Brownian perturbations in the collective motions. This and other experimental evidence indicate that the time evolution of the intermediate complex

may be diffusive in nature and describable in terms of the Master Equation or its equivalent, the Fokker-Planck equation.[3,18,19])

Utilizing a simple diffusion model which specifies the time evolution of the mass asymmetry degree of freedom and incorporates a simple dynamical representation of the deep inelastic collision process, the charge and angular distributions from ^{197}Au and ^{181}Ta targets + 620 MeV ^{86}Kr reactions have been semiquantitatively reproduced. In addition, the broader charge distributions and the forward peaked angular distributions observed in the ^{86}Kr + ^{107,109}Ag system[16]) have also been qualitatively explained in terms of this model. To further investigate the transition region between the light and heavy targets and to determine whether this diffusion model would quantitatively describe the observed phenomena over the mass region from ^{107,109}Ag to ^{197}Au with a consistent set of parameters, we have investigated the ^{86}Kr + ^{159}Tb system and performed diffusion model calculations for this system plus the previously studied ^{86}Kr + ^{107,109}Ag system.

In this report a brief description of the experimental technique is given in section 2. Section 3 contains the experimental results and section 4 briefly describes the diffusion model. A comparison of the theoretical calculations and the experimental data is given in section 5.

2. Experimental Technique

2.1 PROCEDURE

A beam of 620 MeV ^{86}Kr ions from the Lawrence Berkeley Laboratory SuperHILAC was utilized to bombard natural, self-supporting ^{159}Tb targets. To minimize the possibility of target breakage, the maximum beam intensity was limited to 20 nA (q = +32). Reaction products were detected with four telescopes[20]) mounted in pairs on opposite sides of the scattering chamber, each consisting of a gas ionization ΔE counter and a 300 μm solid state E counter. Two parameter (ΔE,E) event-by-event data were taken with a multiplexer, analog-to-digital converter system and written on magnetic tape for later off-line analysis.

The gas counters were operated with pure methane (CH_4) gas at pressures between 50 and 300 Torr. These pressures were regulated to better than 0.5% with Cartesian manostats. The telescope acceptance angles, which ranged from 1° to 2.5°, were defined by circular collimators of 1 to 3 mm in diameter. The absolute solid angles of the telescopes were determined with an ^{241}Am α source of known activity. In order to determine the scattering chamber asymmetry, elastic scattering measurements were made at both positive and negative angles.

An energy calibration of the E amplifier systems was obtained from a precision mercury pulser that was calibrated at low energies with an ^{241}Am α source and at high energies with elastically scattered ^{86}Kr ions. The ΔE amplifier systems were calibrated by utilizing the mercury pulser and measuring the shift of the elastic scattering peak in the E detector (and the corresponding amplitude in the ΔE detector) for runs with and without gas in the telescope. The measured laboratory energies of the

detected fragments were corrected for losses in the target, gas windows, and the dead layer of the solid state counter using polynomial fits to Northchiffe & Schilling range-energy data[21]) as well as for the pulse-height defect[22]) in the solid state counter. Although the relative energies are known to better than 1%, because of the uncertainties in the absolute beam energy and in the above corrections, the total laboratory energy of a fragment could be in error by up to 3%.

2.2 DATA ANALYSIS

The event-by-event data was sorted off-line into two-dimensional ΔE vs. E maps. In the ΔE-E plane, events having the same Z but different energies lie along a ridge, that of the projectile (Z = 36) being the most prominent. Figure 1 clearly depicts the individual ridges and valleys for elements from Z = 22 to 44 and shows weaker evidence for those of the even heavier elements. To systematically determine these ridges, a computerized technique[23]) was used to automatically locate the maxima along a given E column. The grid of ridge points generated by these maxima defined the Z-ridges (see dashed lines in fig. 1). The limits for individual elements were chosen midway between these ridge lines.

To further illustrate the ability of this ΔE-E telescope to identify the atomic number of an event, the distance between adjacent Z ridges was divided into 10 bins and any event falling within such a bin assigned the appropriate fractional atomic number. The data shown in fig. 1 have been replotted in fig. 2 as the number events for each fractional Z-value with a lower energy threshold, to eliminate contamination of the Z-bins by unresolvable heavier elements of very low energy (see fig. 1). Elements below the projectile are clearly resolved where adequate statistics are available. Above the projectile, the peak-to-valley ratio for individual

elements decreases from 2/1 until it reaches unity at Z = 45, but then increases above unity for Z = 48 to 52, enabling an accurate interpolation for the location of the intermediate Z-ridges. Since the elemental resolution is not perfect, tailing into adjacent Z-bins exists, particularly for the higher Z-values. However, for each Z-bin the average Z-value is well determined over the observed energy range.

3. Experimental Results

In this section center-of-mass kinetic energy spectra, charge and angular distributions are presented for over 25 identified elements. The number of identified elements is dependent on the fragment kinetic energy, with the largest number resolvable at forward angles where the laboratory energies are the highest.

3.1 KINETIC ENERGY SPECTRA

To generate kinetic energy spectra for each identified element, a two dimensional gate was set around each element ridge and laboratory energy spectra were projected out. These spectra were transformed to the center-of-mass system utilizing the charge-equilibrium model[24]) to calculate the pre-evaporative fragment mass. The effect of light-particle evaporation (n, p and α) on the fragment masses and energies was neglected (corrections due to this effect are estimated to be < 10%, see discussion in ref. 14). Typical c.m. kinetic energy spectra for representative elements at four lab angles are shown in fig. 3. Spectra for elements which are the same number of charge units removed from the projectile Z are very similar, and are shown in the same column (see i.e. Z = 34 & 38 and 30 & 42). For elements 6 or more charge units removed from the projectile, a single peak is observed at each angle with a mean energy slightly below the Coulomb barrier ($\sim$ 150 MeV).

Although these Gaussian shaped peaks decrease in amplitude with angle, their shape is approximately independent of angle.

The energy spectra of elements within 4 charge units of the projectile Z show a dramatic shape dependence on angle. At 10° the spectra (solid circles) consist of a single-relaxed component peaked at energies near the Coulomb barrier. At 20° (nearer the grazing angle, 33° lab) the spectra (squares) broaden toward higher energies. Very near the grazing angle (see 30° data, triangles), the spectra show evidence for an unresolved relaxed component and a partially-damped (or quasi-elastic) component which peaks at near-elastic energies. For angles well behind the grazing (see 45° data, open circles), the quasi-elastic component vanishes, and these spectra resemble the very forward angle ones.

The overall dependence of the energy spectra on atomic number and angle for the ^{159}Tb + 620 MeV ^{86}Kr reaction is intermediate to that observed for heavier targets[14,15] (like ^{181}Ta and ^{197}Au) and a lighter target[16] (like ^{107,109}Ag). For the ^{181}Ta and ^{197}Au targets, the relaxed and quasi-elastic components strongly overlap at the grazing angle for elements near the projectile, whereas for the ^{159}Tb target there is less overlap (see 30° data, triangles in fig. 3). For the ^{107,109}Ag target[16] the two components become clearly separated. The above trend has been correlated[3,25] with the ratio (E/B) of the center-of-mass energy to the Coulomb barrier[26] for the entrance channel which increases from 1.5 to 1.9 as the target mass decreases from ^{197}Au to ^{107,109}Ag for 620 MeV ^{86}Kr.

In ref.25 a simple model has been used to show that the ratio E/B is proportional to the mean rotational angle of the intermediate complex which is given by the product of its mean lifetime and rotational velocity.

This model also predicts that the mean lifetime of the intermediate complex increases as the ratio E/B increases. (For larger values of E/B there is more energy above the barrier and the fragments can undergo greater interpenetration.) Thus for the $^{197}Au + ^{86}Kr$ system where E/B is 1.5, the rotational period (90×10^{-22}S) of the intermediate complex is long, due to a large moment of inertia, and the mean lifetime much smaller (35×10^{-22}S) so that little rotation occurs before its decay.

For this system the yield for a range of ℓ-values is focussed around the grazing angle. Although the ℓ-dependent lifetime causes the intermediate complex formed by the smaller ℓ-waves to rotate through a larger angle, this effect is compensated by the more backward formation angle for these smaller impact parameters. A continuous transition is observed from quasi-elastic down to relaxed energies in the energy spectra because of this focussing of the yield from a wide range of ℓ-waves, and because the tangential kinetic energy is only partially dissipated while the radial kinetic energy is almost completely dissipated. For the $^{107,109}Ag$ target, where E/B is 1.9, the rotational period of the intermediate complex is shorter due to its smaller moment of inertia and its mean lifetime is longer so that at the grazing angle the yield is depleted of partially-damped events (intermediate lifetimes) since for these events the dinuclear system lives long enough to rotate to more forward angles or even through 0° before decaying. Therefore, only events which result from the decay of a very short lived (little energy damping) or a relatively long lived (full energy damping) intermediate complex are observed near the grazing angle. Thus as E/B increases, the quasi-elastic and the relaxed component appear to separate in energy near the

grazing angle because of the depletion of events of intermediate damping. This effect is evident in the Wilczynski diagrams[27]) of ref. 16

At this point it should be noted that more detailed studies[28]) indicate that the projection of the deflection function onto the $E_T - \theta$ plane is more complicated than implied in the standard Wilczynski picture. Such a projection may in fact move from positive to negative angles and then back again to positive angles.

Extracted mean c.m. energies (circles) and FWHM's (squares) are presented in fig. 4 for the detected elements. These values were obtained by averaging over the angular range of measurements where the quasi-elastic component was absent. The "error bars" represent one standard deviation from the mean value. For comparison a solid curve is given corresponding to the calculated[26]) Coulomb repulsion energies for two nearly touching spherical fragments. As was observed for the ^{197}Au, ^{181}Ta and ^{107,109}Ag targets[14-16]), these mean energies follow the trend of, but fall below, the calculated energies. The experimental c.m. energies have not been corrected for particle evaporation (see earlier discussion), and the solid curve does not include the rotational energy of the complex[7]) . However, because these two effects are similar in magnitude, their net effect should not appreciably change the separation between the data points and the calculated curve. The observed FWHM ($\sim$ 45 MeV) are approximately constant as a function of atomic number and are comparable to those measured for Kr-induced reactions on other targets.

3.2 CHARGE DISTRIBUTIONS

Laboratory charge distributions integrated over energy are presented in fig. 5. Because the relaxed and quasi-elastic components were not

clearly separated in the energy spectra (see fig. 3), both have been included. One should note that for all elements except for a few near the projectile, the maximum cross section occurs at forward angles and rapidly decreases with increasing angle. Furthermore, the broad shape of the charge distributions at the most forward angles narrows as the grazing angle is approached and then flattens into a very broad distribution at backward angles with an apparent shift of the centroid to higher Z-values. Similar patterns have been observed in 620 MeV ^{86}Kr bombardments of other targets[14-16], with these distributions from the ^{159}Tb target being intermediate in character relative to those from the ^{107,109}Ag and ^{197}Au targets[14-16]. The increased cross section for elements above the projectile relative to those below can be explained by a driving potential which enhances diffusion toward symmetry, Z = 50 (see discussion in section 4).

3.3 ANGULAR DISTRIBUTIONS

Center-of-mass angular distributions for atomic numbers between 24 and 48 are presented in fig. 6. Because of serious background problems from slit scattering, data for the projectile (Z=36) have been omitted. Distributions for the same net charge transfer to and from the projectile are shown in adjacent columns, with the number of protons transferred increasing from 1 to 12 as one goes down a column. For the same amount of charge transfer, the angular distributions are very similar in shape (i.e. see Z = 31 and 41); however, the elements above the projectile have substantially larger cross sections as a result of a driving potential, which favors diffusion toward symmetry. As the number of transferred charge units increases, the side peaking observed at 50° for Z = 35 and

37 decreases in magnitude, and the position of this peak moves to smaller angles, producing first a shoulder for intermediate charge transfers, and eventually disappearing for larger charge transfers, leaving forward peaked distributions in excess of the $1/\sin\theta$ compound nucleus limit. For comparison a $1/\sin\theta$ angular distribution is shown at the bottom of the second column. Similar patterns[14,15]), but with more intense side peaking, have been observed in ^{86}Kr induced reactions at 620 MeV on ^{181}Ta and ^{197}Au targets. This side peaking phenomena is believed to result because for each of the above systems the lifetime of the intermediate complex is much shorter than its rotational period causing fragments to be preferentially emitted on the side of impact. In addition, the time scales are matched so that the two effects due to the decreasing lifetime and decreasing angle of formation of the intermediate complex with increasing ℓ-wave compensate and cause a focussing of the yield near the grazing angle.

The continuous transition from side peaking to forward peaking with increasing charge transfer is explained in terms of a diffusion controlled time delay[13]). On the average in a diffusion process, small charge transfers require less time than larger ones. Since small charge transfers populate elements near the projectile, the effective lifetime is short, resulting in side peaked angular distributions. For larger charge transfers, the longer effective lifetimes allow for more rotation of the complex before decay, producing forward peaked angular distributions.

4. Diffusion Model

In this section the diffusion model of Moretto and Sventek[17]) will be briefly described (see refs. 3,17 and 18 for a more complete description and justification of this model). The target and projectile are assumed to approach each other on Coulomb trajectories which are determined by the total energy (including Coulomb) of the system. During the collision process, which is assumed to occur on a time scale short compared to the diffusion time, the incoming kinetic energy is damped into internal degrees of freedom, giving rise to a "warm" system, and the neutron-to-protron ratio is equilibrated. (No slippage angle[17]) is assumed to minimize the number of adjustable parameters).

After the fast initial collision stage, a rotating intermediate complex of well-defined mass asymmetry is formed. A diffusion process, which occurs on a time scale comparable to that of the rotational period of the intermediate complex, regulates the exchange of mass between the two touching fragments, thus generating a time-dependent distribution of asymmetries for the intermediate complex. After rotation through an angle, which is determined by its lifetime (an angular momentum dependent lifetime is assumed which decreases for increasing ℓ) and angular velocity, the complex decays into two fragments which separate on Coulomb trajectories determined by the sum of their Coulomb and rotational energies. The assumption of the completion of the energy dissipation stage before mass transfer begins is, to be sure, a simplification. It should be stressed that this assumption has been made to make the calculations tractable and to avoid the introduction of more adjustable parameters, and as such, it should not be considered fundamental to the model.

The mass exchange between the two segments of the intermediate complex has been treated by Moretto and Sventek as a diffusion process which is governed by the Master equation:

$$\dot{\phi}_Z(t) = \sum_{Z'} \Lambda_{ZZ'}\phi_{Z'}(t) - \Lambda_{Z'Z}\phi_Z(t) \qquad (1)$$

where $\phi_Z(t)$ is the population of configuration Z at time t, $\dot{\phi}_Z(t)$ is the time derivative of ϕ and $\Lambda_{ZZ'}$ is the macroscopic transition probability coupling the configurations Z and Z'.

The macroscopic transition probabilities can be defined:

$$\Lambda_{ZZ'} = \lambda_{ZZ'}\rho_Z \qquad (2)$$

$$\Lambda_{Z'Z} = \lambda_{Z'Z}\rho_{Z'} \qquad (3)$$

in terms of a microscopic transition probability $\lambda_{ZZ'}$ (which is symmetric because of microscopic reversibility)

$$\lambda_{ZZ'} = \lambda_{Z'Z} \qquad (4)$$

and the statistical weights (ρ_Z and $\rho_{Z'}$) of the macroscopic configurations. These statistical weights can be identified with the level densities of the complex:

$$\rho_Z = \rho(E-V_Z) \quad , \qquad (5)$$

where E is the total energy of the system and V_Z is its potential energy. For small V_Z , one can expand the level density as follows[17]):

$$\rho(E - V_Z) = \rho(E)\ \exp[-V_Z/T] \qquad (6)$$

where the quantity T can be identified with the thermodynamic temperature.

The microscopic transition probability $\lambda_{ZZ'}$ can be rewritten[17]):

$$\lambda_{ZZ'} = \frac{\kappa f}{\sqrt{\rho_Z \rho_{Z'}}} \quad , \tag{7}$$

in terms of a diffusion constant κ and a form factor f which is set equal to the window open between the two fragments:

$$f = \frac{2\pi R_1 R_2 d}{R_1+R_2} \quad , \quad (d = 1.0 \text{ fm}) \quad . \tag{8}$$

In the spirit of the independent particle model, the sum over Z' in Eq. 1 can be restricted to values of $Z' = Z \pm 1$. Utilizing the above equations, the Master Equation can be rewritten as:

$$\dot{\phi}_Z(t) = \sum_{Z'=Z\pm1} \frac{\kappa f}{\exp\left[-\frac{V_Z+V_{Z'}}{2T}\right]} \times \left[\phi_{Z'}\exp(-V_Z/T) - \phi_Z \exp(-V_{Z'}/T)\right] . \tag{9}$$

A key quantity in the above expression is the potential energy of the intermediate complex V_Z, which controls the time evolution of the mass asymmetry mode. It can be computed from the liquid drop model:

$$V_Z = E_{LD}(Z) + E_{LD}(Z_{tot} - Z) + E_{Coul} + E_{rot} \quad , \tag{10}$$

where the first two terms are the liquid drop energies of the two fragments and the last two terms are the Coulomb repulsion and rotation energies, respectively. For simplicity the fragments are assumed to be spherical in shape, but are allowed to overlap. The distance between their centers D is given by

$$D = R_1 + R_2 + \delta \quad , \tag{11}$$

where R_1, R_2 are the fragment radii (r_0 = 1.225) and δ is an adjustable overlap parameter. Potential energy curves, as a function of the system (^{159}Tb + 620 MeV ^{86}Kr) asymmetry calculated for several ℓ-waves with δ = -2.0 fm are presented in fig. 7. The potential energy for each asymmetry has been calculated relative to the injection point (Z = 36). For the low (ℓ = 0 - 80) angular momenta, the potential energy of the complex is essentially flat over a broad region of asymmetries around the injection point and thus diffusion is equally probable to smaller or larger asymmetries. As the angular momentum increases, a potential minimum develops at symmetry (Z = 50) which becomes very pronounced for the highest ℓ-waves. This minima and the negative slope of the potential at the injection point for the higher ℓ-waves, enhances diffusion toward symmetry and inhibits the population of elements below the projectile.

Utilizing Eqs. 9 and 10 population probabilities were calculated as a function of the interaction time for several ℓ-waves (ℓ_{max} = 266 $\hbar$) and are shown as contour plots in the Z-t plane in fig. 8. These diffusion model calculations utilized the potential energy curves given in fig. 7. At time zero only one asymmetry exists (target and projectile). For small values of t, elements on either side of the projectile and target are quickly populated. For larger ones the two distributions overlap and merge into a single symmetric distribution. The flat ℓ = 0 potential (see fig. 7) creates a very broad Z-distribution (see fig. 8). Larger ℓ-values result in progressively narrower Z-distributions because the nuclear temperature of the complex is reduced as more energy is tied up in rotation, and because diffusion toward very small and very

large asymmetries is inhibited by the parabolic-shaped driving-potential centered around symmetry. The enhanced diffusion towards symmetry with increasing ℓ is beautifully illustrated in the shorter times required for the target and projectile distributions to merge for larger ℓ. In summary, these calculations predict broad charge distributions for low ℓ-waves and sharper ones for high ℓ-waves. The experimental observations of broad charge distributions before and behind and narrow ones near the grazing angle corroborates the previously established correlation between laboratory angle and ℓ-value [13,14].

In order to make quantitative comparisons with the experimental data, it is necessary to make some assumptions about the distribution of lifetimes $\pi(t,\ell)$ for the intermediate complex. It was assumed[3,18] that

$$\pi(t,\ell) = \frac{1}{N(\ell)} \exp\left[-(t-\tau(\ell))^2/\sigma^2(\ell)\right] \quad , \tag{12}$$

where $N(\ell)$ is a normalization constant and $\tau(\ell)$ and $\sigma^2(\ell)$ are given by

$$\tau(\ell) = \tau(0)(1 - \ell/\ell_{max}) \quad , \tag{13}$$

$$\sigma^2(\ell) = \sigma^2(0)(1 - \ell/\ell_{max}) \quad , \tag{14}$$

where $\tau(0)$ is the mean lifetime and $\sigma(0)$ is the spread in the lifetimes for $\ell = 0$. The assumption of a linear ℓ-dependence for $\tau(\ell)$ and $\sigma^2(\ell)$ has been made in the spirit of simplicity. The essential point to be made about τ and σ^2 is that they decrease with increasing ℓ, rather than the details of that dependence. Utilizing these assumptions, diffusion model calculations of the integrated charge distribution and of the angular distributions have been performed and will be compared with the data in the next section.

5. Comparison of Theory and Experiment

5.1 INTEGRATED CHARGE DISTRIBUTIONS

To test whether the diffusion model could successfully describe with a consistent set of parameters, the charge and angular distributions produced from ^{86}Kr induced reactions on targets ranging from ^{107,109}Ag to ^{197}Au, we have performed calculations for 620 MeV ^{86}Kr induced reactions on ^{159}Tb and ^{107,109}Ag. Previously, calculations with this model semiquantitatively reproduced data from ^{181}Ta and ^{197}Au targets with the following parameters values[14,15]):

$$\tau(0) = 35. \times 10^{-22} \text{ sec} ,$$

$$\sigma(0) = 10. \times 10^{-22} \text{ sec} ,$$

$$\kappa = 0.5 \times 10^{21} \text{ fm}^{-2} \text{ sec}^{-1} ,$$

$$\delta = -2.0 \text{ fm} .$$

Diffusion model calculations of the angle integrated charge distributions from the ^{159}Tb target utilizing the values given above (solid curve) are presented in fig. 9. The experimental values (solid circles) in fig. 9 were obtained by integrating over the experimental range of measurements. Because of the limited angular range of the measurements and the steeply falling angular distributions for large charge unit transfers, a sizable fraction of the cross section has been missed. (Forward angle data requires long counting times because the large elastic rate severely restricts the beam intensity.) This fact can account for the experimental values being lower than the calculations for the low and high Z values; if one extrapolates the experimental data using the shapes of the theoretical angular distributions (see fig. 10), the discrepancy is

reduced to about 20%. Near Z = 36 the calculations grossly overestimate the cross section. However, this disagreement occurs because the model in its present form is not readily applicable[18]) to the partially damped events which, as the energy spectra for these elements show, are abundant near the grazing angle. In particular, the overlap parameter δ and the form factor f have been held constant for all ℓ-values. Since both of these quantities are expected to decrease for high ℓ-waves, a fact that the present model does not take into account, the highest ℓ-waves have been left out of the calculations ($P(\ell) = 0.5$ for $\ell = 250\,\hbar$, where $\ell_{max} = 266\,\hbar$). (It should be noted that no lower ℓ-cutoff was assumed in the calculations.)

Since the potential energy of the intermediate complex is sensitive to the shape of the complex, we investigated this dependence by varying the overlap parameter δ. Diffusion model calculations for two smaller values of δ (dashed lines) are also shown in fig. 9. Decreasing the overlap parameter from -2.0 to -1.0 fm shifts cross section from elements below the projectiles to those above it. This shift occurs because, for the smaller overlap parameter, the potential energy of the intermediate complex is steeper at the injection point, inhibiting diffusion to greater asymmetry and favoring diffusion toward symmetry. Because of the arguments enumerated above, it is felt that the calculations with $\delta = -2.0$ fm best reproduce the data. Since this value also gave good agreement with the integrated charge distributions from the ^{181}Ta and ^{197}Au targets, it seems to be target independent over a large mass range for Kr-induced reactions.

5.2 ANGULAR DISTRIBUTIONS

5.2.1. ^{159}Tb + 620 MeV ^{86}Kr. To more rigorously test the diffusion model, calculations of the angular distributions were performed with the parameters (δ = -2.0, $\tau(0)$ = 35, $\sigma(0)$ = 10 and κ = 0.5) which gave the best fit to the data from the ^{181}Ta and ^{197}Au targets. In fig. 10 an absolute comparison is made between the experimental (solid circles) and the calculated (curves) angular distributions for representative elements produced in the ^{159}Tb + 620 MeV ^{86}Kr reaction. The overall agreement between the theoretical predictions and experiment is quite good with both the shape and magnitude being reproduced for elements 3 or more Z's above the projectile and 5 or more below. In particular, the calculations reproduce the observed transition from side-peaked distributions near the projectile Z to forward peaked ones as the number of protons transferred is increased. Although the calculations indicate substantially less side peaking than is observed for elements adjacent to the projectile, most of this side peaking is due to the quasi-elastic process, which the present calculation neglects. However, the overall fall off of the cross section from forward to backward angles is well reproduced. To illustrate that these cross sections are more forwarded peaked than the compound nucleus limit, a 1/sin θ curve is included in the bottom right colum. One should note that since the value for $\tau(0)$ of 35 x 10^{-22} S is smaller than that of the rotational period (77×10^{-22} S) of the intermediate complex, the yield observed at angles behind the grazing angle is due to small impact parameters and not rotation through 0°.

5.2.2. ^{107,109}Ag + 620 MeV ^{86}Kr. An extensive discussion of the ^{107,109}Ag + 620 MeV ^{86}Kr system has been presented by Schmitt et al. in ref. 16. This investigation demonstrated that these experimental charge and angular distributions are dramatically different from those observed in ^{86}Kr induced reactions on heavier targets like ^{181}Ta and ^{197}Au. In particular the charge distributions are very broad and the angular distributions are essentially forwarded peaked. This broadening of the charge distributions and weakening of the side peaking in the angular distributions as one goes from ^{197}Au to ^{107,109}Ag targets was explained qualitatively in terms of the diffusion model and was attributed to a longer mean lifetime for the latter system. Because no quantitative diffusion model calculations were available when ref. 16 was published, and because subsequently the diffusion model with a single set of parameters has been able to semiquantitatively reproduce the measured data from three targets over a mass range from 159 to 197, it is interesting to determine if these same parameters will reproduce the ^{107,109}Ag + 620 MeV ^{86}Kr data or whether a longer lifetime will be required as predicted by E/B systematics.[25])

To this end angular distributions (solid curves) were calculated for fragments produced in the reaction ^{107,109}Ag + 620 MeV ^{86}Kr utilizing the parameters which gave the best fits to the data from the three heavier targets and are presented with the experimental data (solid circles) in fig. 10. Although the overall agreement with the data is somewhat poorer than that obtained for the other systems with these same parameters, the calculations do reproduce the forward angle region for several Z values around the projectile. However, for elements 31-27

this region is somewhat overestimated by the calculations. In addition, the backward angle region is consistently underestimated. These two features indicate that the intermediate complex's lifetime is too short so that the complex does not rotate far enough before decaying. With a longer mean lifetime the complex can rotate substantially through 0° and thus yield will be shifted from forward angles to more backward ones.

To determine if increasing the lifetime would give a better fit to the data, calculations (dashed lines) were performed for $\tau(0) = 55$. For Z values several charge units removed from the projectile, this longer lifetime gives a better fit to the data. Although the yield at backward angles is consistently overestimated (except for Z = 25), the slower fall off with angle is reproduced with $\tau(0) = 55$. An intermediate value for the lifetime of 45×10^{-21} S would increase the backward angle yield relative to $\tau(0) = 35$ by increasing somewhat the angle reached by rotation through 0°, but would not so deplete the forward angle yield. Thus it seems that the $^{107,109}Ag$ + 620 MeV ^{96}Kr system would be best described by increasing the intermediate complex lifetime by 30%. Such an increase is in fact predicted by a very simple model[25]) which predicts that the lifetime of the intermediate complex increases as the ratio E/B increases.

6. Conclusion

A systematic investigation of Kr induced reactions at 620 MeV on targets covering a large mass range has demonstrated that the character of the charge and angular distributions change dramatically when the target mass is decreased from 197 to 108. By investigating a target (^{159}Tb) midway between A = 197 and 108 and successfully reproducing the experimental data and the previously published ^{107,109}Ag data with diffusion model calculations utilizing a consistent set of parameters which also fit the data from the heavier ^{181}Ta and ^{197}Au targets, we have demonstrated the broad applicability of this simple model and its ability to quantitatively describe the observed deep inelastic phenomena.

In particular, it seems that the disappearance of the side peaking observed when one goes from Au to Ag is due to the decreasing moment of inertia and the increasing mean lifetime of the intermediate complex. Thus there is much more rotation through 0° for a lighter complex, resulting in a weakening of the side peaking, followed by forward peaking and then a flattening of the angular distributions as more backward angles are populated.

Even though the initial damping of the projectile kinetic energy is neglected in this model, the good fits to the angular distributions for moderate and large net charge transfers illustrate the importance of the main features of the model: 1) the formation of a rotating dinuclear system with well defined mass asymmetry 2) its diffusive evolution along the mass asymmetry axis and 3) its ℓ-dependent lifetime. The underestimation of the side peaking for small charge transfers by the calculations demonstrates the limitations of the present model and the

need to incorporate a proper dynamical treatment of the coupling of the energy damping and mass transfer during the initial stages of the collision.

Acknowledgments

The authors would like to thank B. Cauvin, P. Russo, R. C. Jared and J. Moulton for their help in acquiring the data, E. Cebellos for his assistance in analyzing the data, and J. S. Sventek for helpful discussions on the diffusion model theory and the use of several of his computer codes for performing the diffusion model calculations.

References

1) J. Galin, D. Guerreau, M. Lefort, J. Péter, X. Tarrago and R. Bastile, Nucl. Phys. A159 (1970) 461

2) A. G. Artukh, G. F. Gridnev, V. L. Mikheev, V. V. Volkov and J. Wilczynski, Nucl. Phys. A215 (1973) 91

3) L. G. Moretto and R. Schmitt, J. de Phys. C-5, 37 (1976) 109 and references therein

4) J. Galin, J. de Phys. C-5, 37 (1976) 83 and references therein

5) W. Nörenberg, Journal de Physique C-5, 37 (1976) 141 and references therein

6) P. Colombani, N. Frascaria, J. C. Jacmart, M. Riou, C. Stéphan, H. Doubre, N. Poffé and J. C. Roynette, Phys. Lett. 55B (1975) 45

7) R. Eggers, M. N. Namboodiri, P. Gonthier, K. Geoffroy and J. B. Natowitz, Phys. Rev. Letters 37, (1976) 324

8) J. Barrette, P. Braun-Munizinger, C. K. Gelbke, H. E. Wegner, B. Zeidman, A. Gamp, H. L. Harney and Th. Walcher, Nucl. Phys. A279 (1977) 125

9) J. Péter, C. Ngô, F. Plasil, B. Tamain, M. Berlanger and F. Hanappe, Nucl. Phys. A279 (1977) 110

10) F. Hanappe, M. Lefort, C. Ngô, J. Péter and B. Tamain, Phys. Rev. Lett. 32 (1974) 738

11) K. L. Wolf, J. P. Unik, J. R. Huizenga, J. Birkelund, H. Freiesleben and V. E. Viola, Phys. Rev. Lett. 33 (1974) 1105

12) M. P. Webb, R. Vandenbosch and T. D. Thomas, Physics Letters 62B (1976) 407

13) L. G. Moretto, B. Cauvin, P. Glässel, R. Jared, P. Russo, J. Sventek and G. Wozniak, Phys. Rev. Lett. 36 (1976) 1069

14) P. Russo, R. P. Schmitt, G. J. Wozniak, R. C. Jared, P. Glässel, B. Cauvin, J. S. Sventek and L. G. Moretto, Nucl. Phys. A281 (1977) 509

15) B. Cauvin, R. P. Schmitt, G. J. Wozniak, P. Glässel, P. Russo, R. C. Jared, J. B. Moulton and L. G. Moretto, Lawrence Berkeley Lab Report #LBL-6506, submitted to Nuclear Physics

16) R. P. Schmitt, P. Russo, R. Babinet, R. Jared and L. G. Moretto, Nucl. Phys. A279 (1977) 141

17) L. G. Moretto and J. S. Sventek, Phys. Lett. 58B (1975) 26 and J. S. Sventek and L. G. Moretto, Phys. Lett. 65B (1976) 326

18) L. G. Moretto and J. S. Sventek, Proc. on macroscopic features of heavy ion collisions, vol. 1, 1976, p. 235; Argonne National Lab Report no. ANL/PHY-76-2

19) W. Nörenberg, Z. Physik A274 (1975) 241

20) M. M. Fowler and R. C. Jared, Nucl. Instr. 124 (1975) 341

21) L. C. Northcliffe and R. F. Schilling, Nucl. Data Tables A7 (1970) 233

22) S. B. Kaufman, E. P. Steinberg, B. D. Wilkins, J. Unik, A. J. Gorski and M. J. Fluss, Nucl. Instr. 115 (1974) 47

23) P. Glässel, R. C. Jared and L. G. Moretto, Nucl. Instr. 142 (1977) 569

24) B. Gatty, D. Guerreau, M. Lefort, J. Pouthas, F. Tarrago, J. Galin, B. Cauvin, J. Girard and H. Nifenecker, Z. Phys. A273 (1975) 65

25) G. J. Mathews, G. J. Wozniak, R. P. Schmitt and L. G. Moretto, Z. Physik, in press

26) These calculations assume that $r_0 = 1.225$ and that the distance R separating the two segments of the intermediate complex at scission is given by $R = 1.225\ (A_1^{1/3} + A_2^{1/3}) + 2.0$ fm

27) J. Wilczynski, Phys. Lett. 47B (1973) 484

28) L. G. Moretto, Lawrence Berkeley Laboratory Report #LBL-6572.

Figure Captions

Fig. 1 A two dimensional ΔE vs E contour map for products detected from the reaction 620 MeV ^{86}Kr and ^{159}Tb at 20° lab angle. The correlation of the number of events with the contour intensity scale is given in the bottom right hand corner of the figure.

Fig. 2 Intensity distribution by atomic number of the fragments detected at 20° lab in a ΔE-E telescope illustrating the excellent elemental resolution attained with this simple two counter detection system.

Fig. 3 Typical c.m. kinetic energy spectra for representative elements detected at four lab angles from the ^{159}Tb + 620 MeV ^{86}Kr reaction.

Fig. 4 Mean c.m. energies (circles) and FWHM's (squares) averaged over the angular range where no quasi-elastic component was present. The "error bars" correspond to one standard deviation from the mean value. The FWHM were computed from the second moment of the spectra assuming a Gaussian peak shape.

Fig. 5 Charge distributions measured at several lab angles. Cross sections for Z = 36 have been omitted due to uncertainties caused by large background contributions from slit scattering.

Fig. 6 Experimental c.m. angular distribution for elements detected from the ^{159}Tb + 620 MeV ^{86}Kr reaction. The curves through the data points are only to guide the eye and have no theoretical significance.

Fig. 7 Calculated liquid drop potential energy curves as a function of charge asymmetry for the $^{159}Tb + ^{86}Kr$ reaction for several ℓ-waves. The potential energies have been plotted relative to the entrance channel value.

Fig. 8 Diffusion model calculations presented as contours of constant cross section in the plane defined by the charge asymmetry coordinate (Z) and its lifetime t of the intermediate complex for several ℓ-values.

Fig. 9 A comparison between the experimental angle-integrated cross section (solid circles) and diffusion model calculations (smooth curves) for fragments ($20 \leqslant Z \leqslant 47$) produced in the reaction ^{159}Tb + 620 MeV ^{86}Kr (see text). Calculations are shown for three values of the overlap parameter δ in fm (see text for units of τ_o and σ_o). The experimental values were obtained by integrating over the experimental range of measurements (see fig. 6).

Fig. 10 Absolute comparison between experimental (solid circles) and calculated angular distributions (solid curve) for representative elements produced from the reaction ^{159}Tb + 620 MeV ^{86}Kr (see text). Statistical error bars are shown when they exceed the size of the data point. The absolute values could be in error by up to 30%.

Fig. 11 Absolute comparison between experimental (solid circles) and calculated (curves) angular distributions for representative elements produced from the reaction $^{107,109}Ag$ + 620 MeV ^{86}Kr. Calculations are presented for two values of $\tau(0)$ the mean lifetime of the intermediate complex for the $\ell = 0$ partial wave.

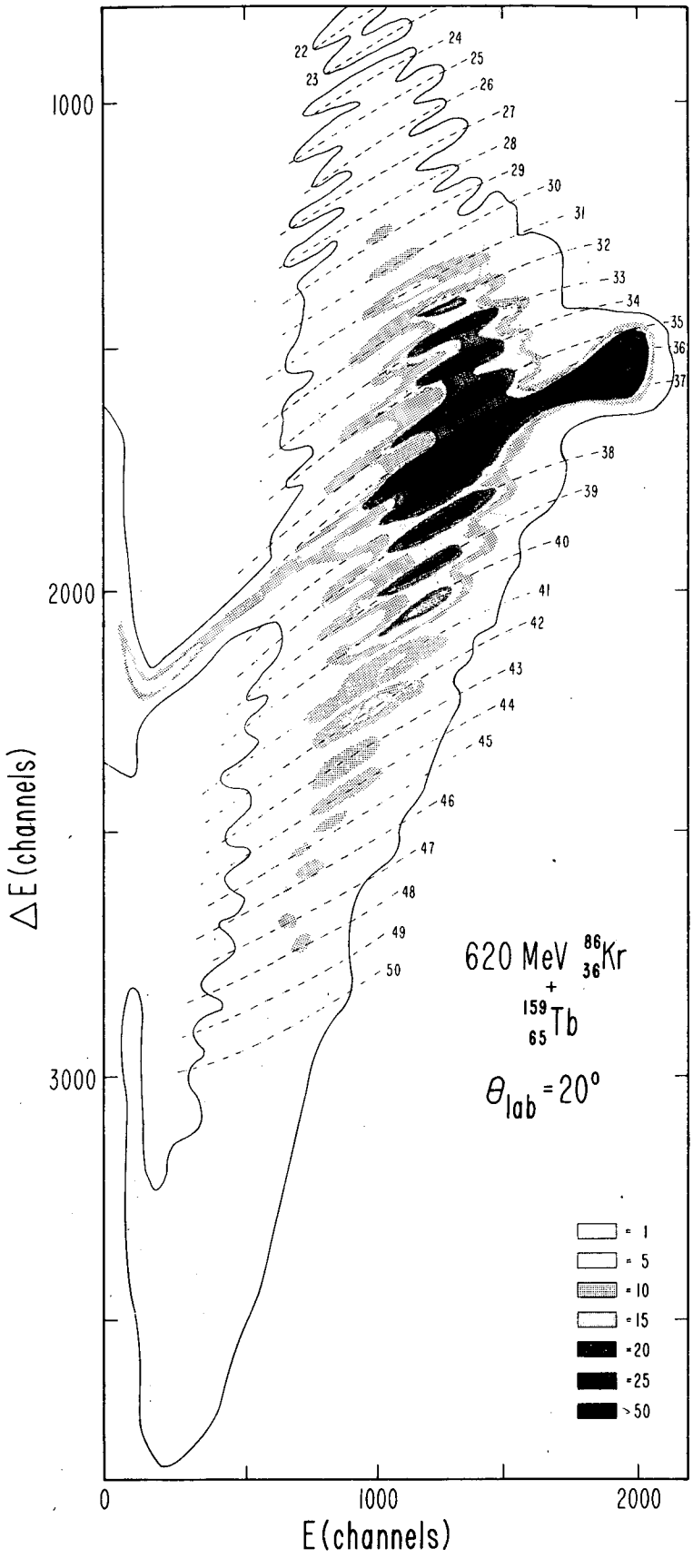

Fig. 1

XBL 76H-4408

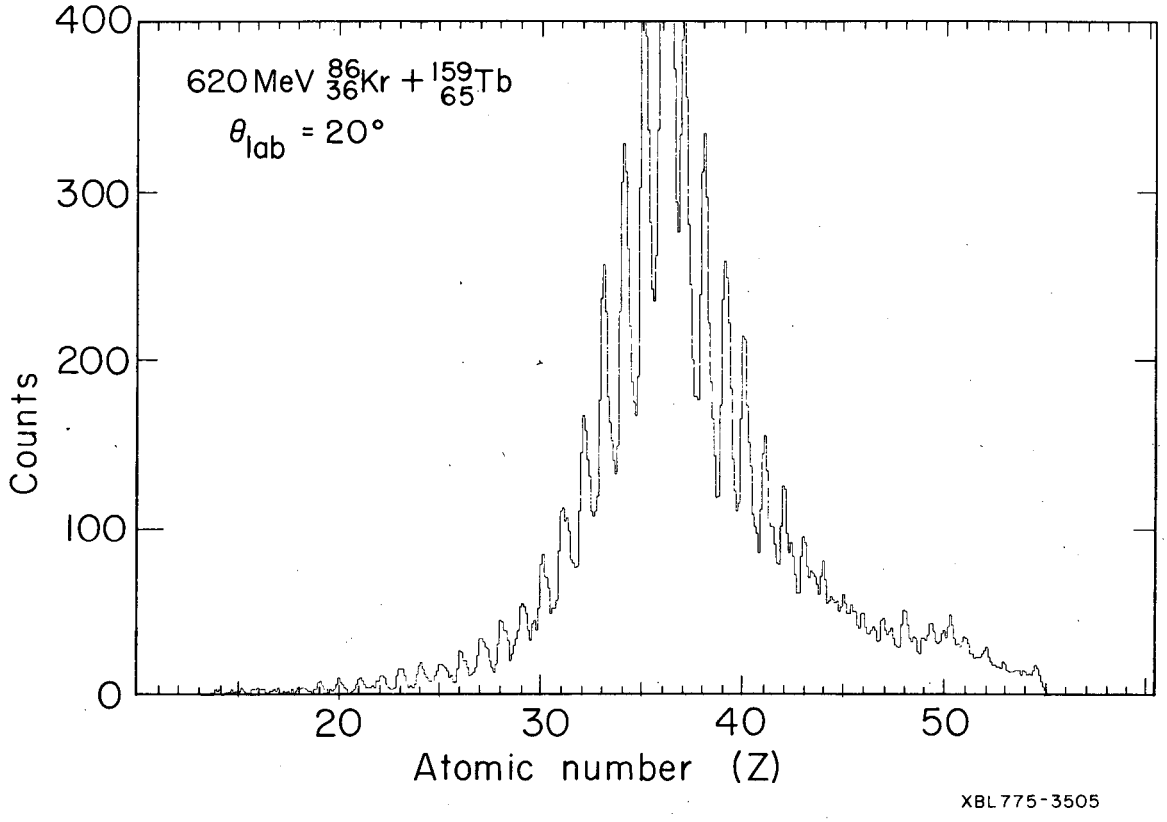

Fig. 2

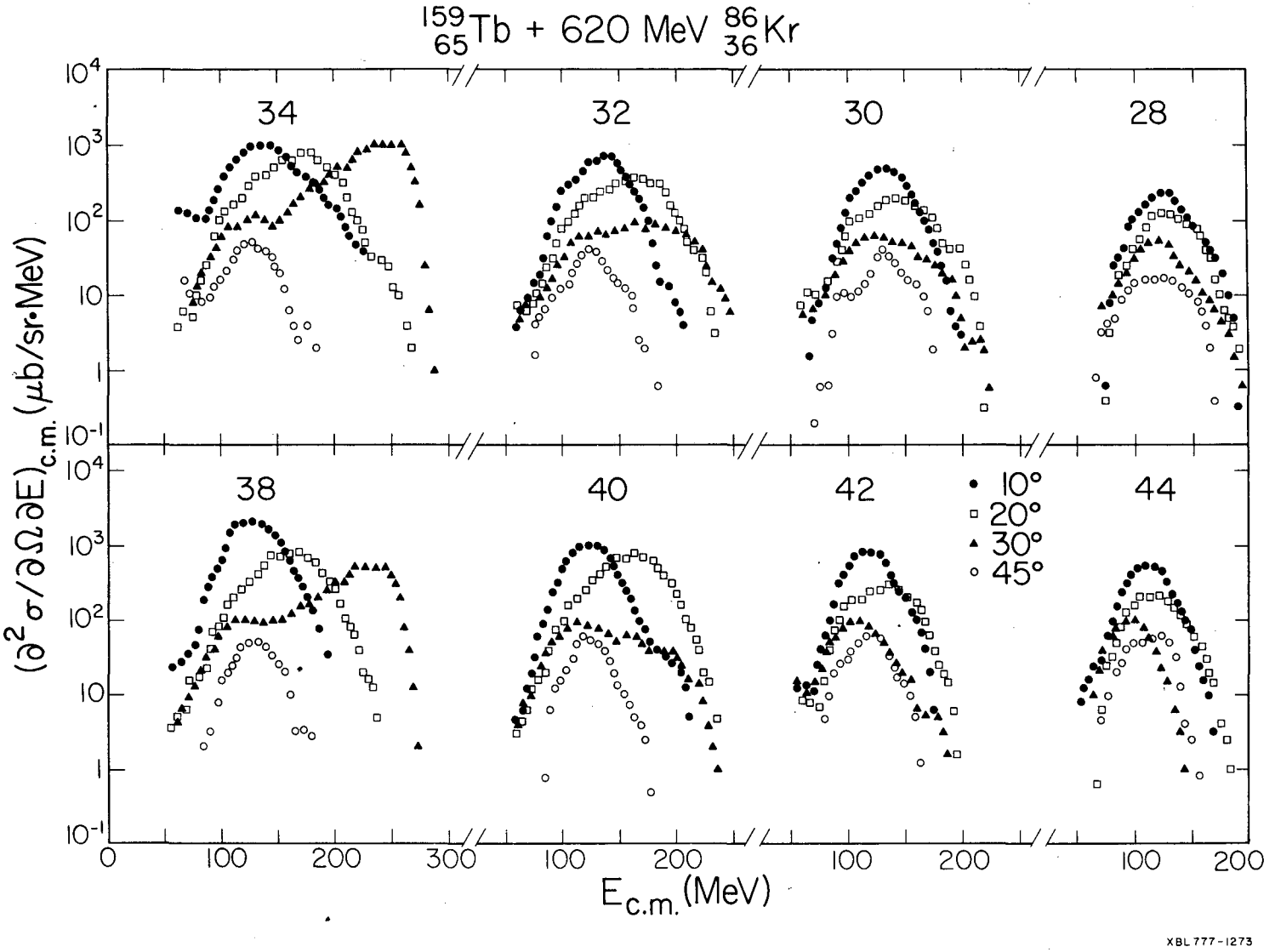
$^{159}_{65}$Tb + 620 MeV $^{86}_{36}$Kr
34
32
30
28
38
40
42
44
10°
20°
30°
45°
$(\partial^2\sigma/\partial\Omega\partial E)_{c.m.}$ (μb/sr•MeV)
$E_{c.m.}$ (MeV)
XBL 777-1273

Fig. 3

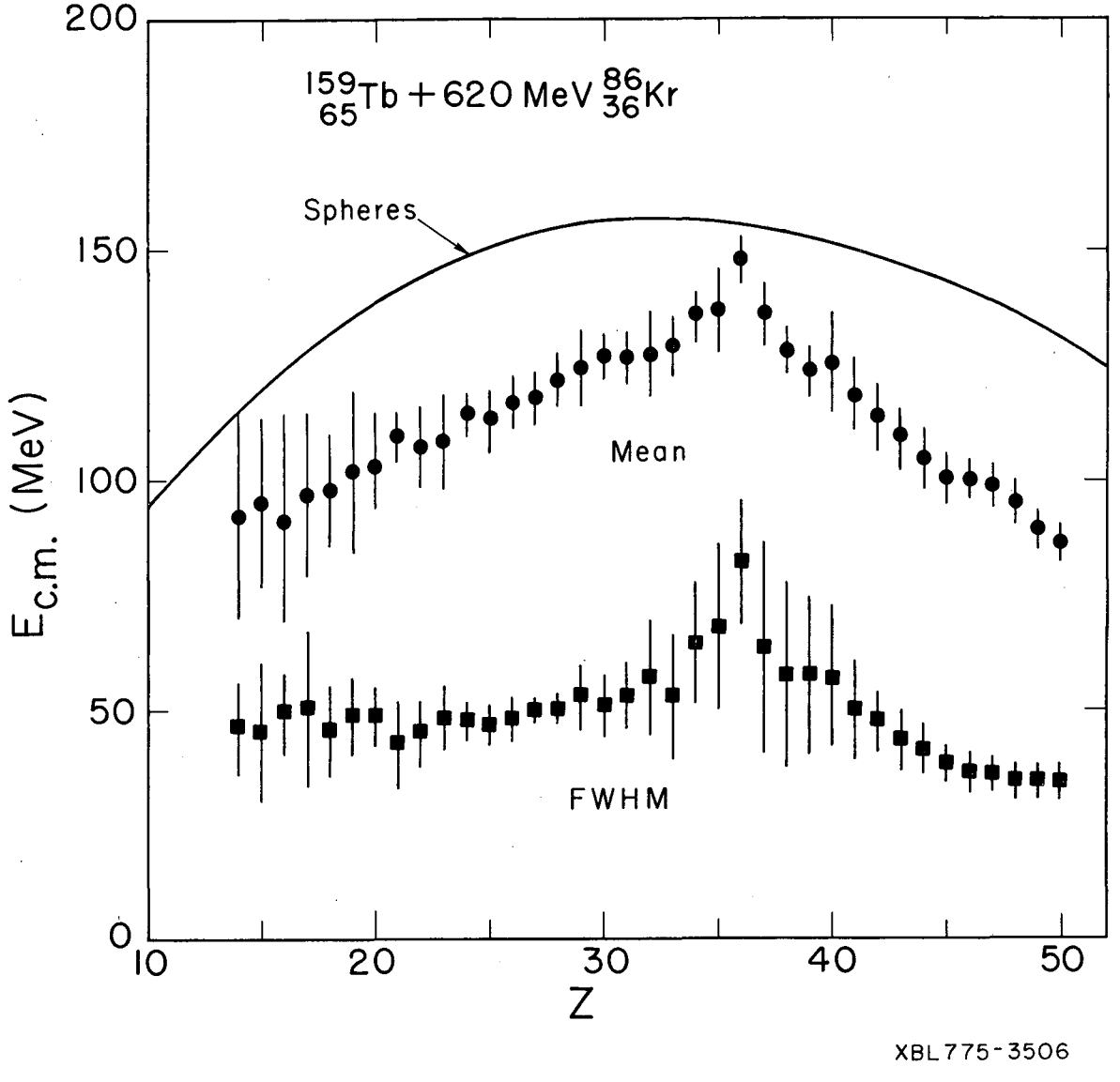

Fig. 4

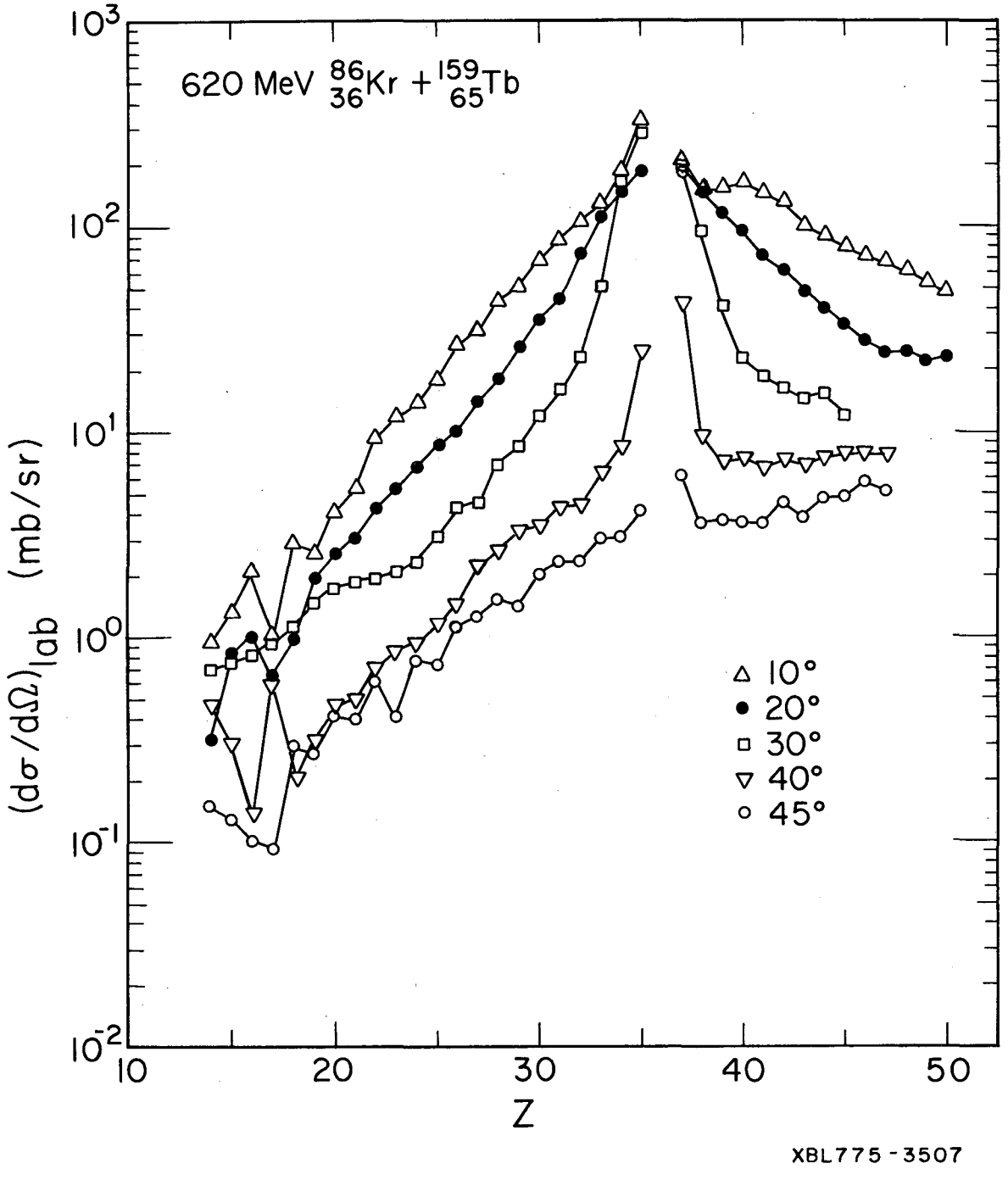
620 MeV $^{86}_{36}$Kr + $^{159}_{65}$Tb
$(d\sigma/d\Omega)_{lab}$ (mb/sr)
Z
10°
20°
30°
40°
45°
XBL775-3507

Fig. 5

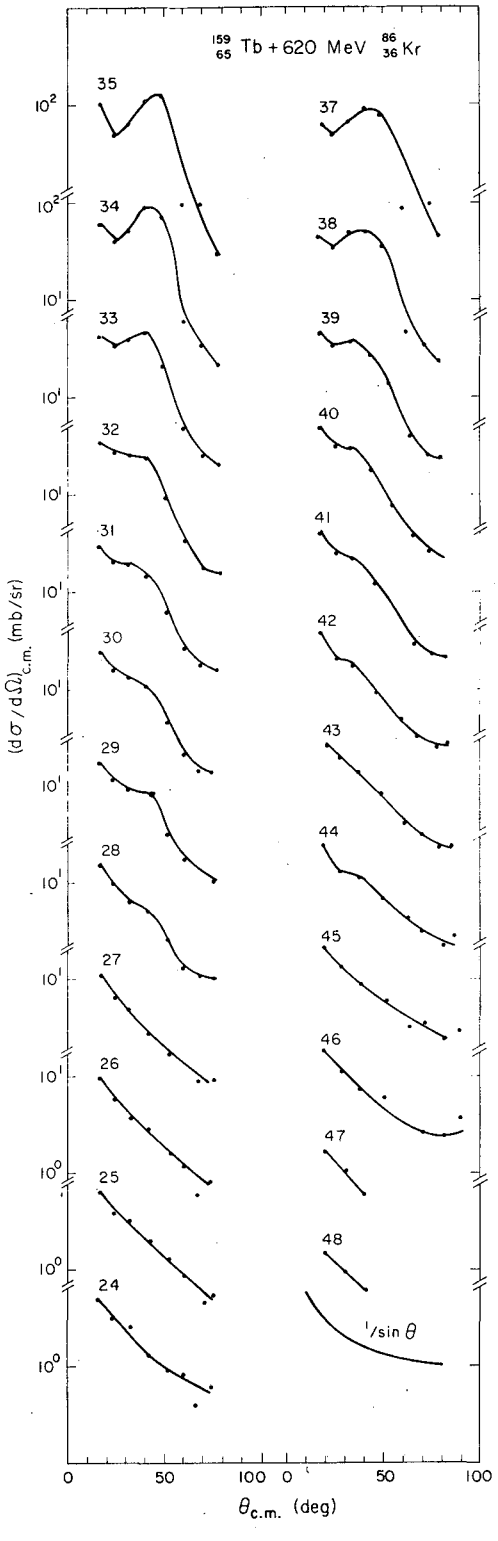

Fig. 6

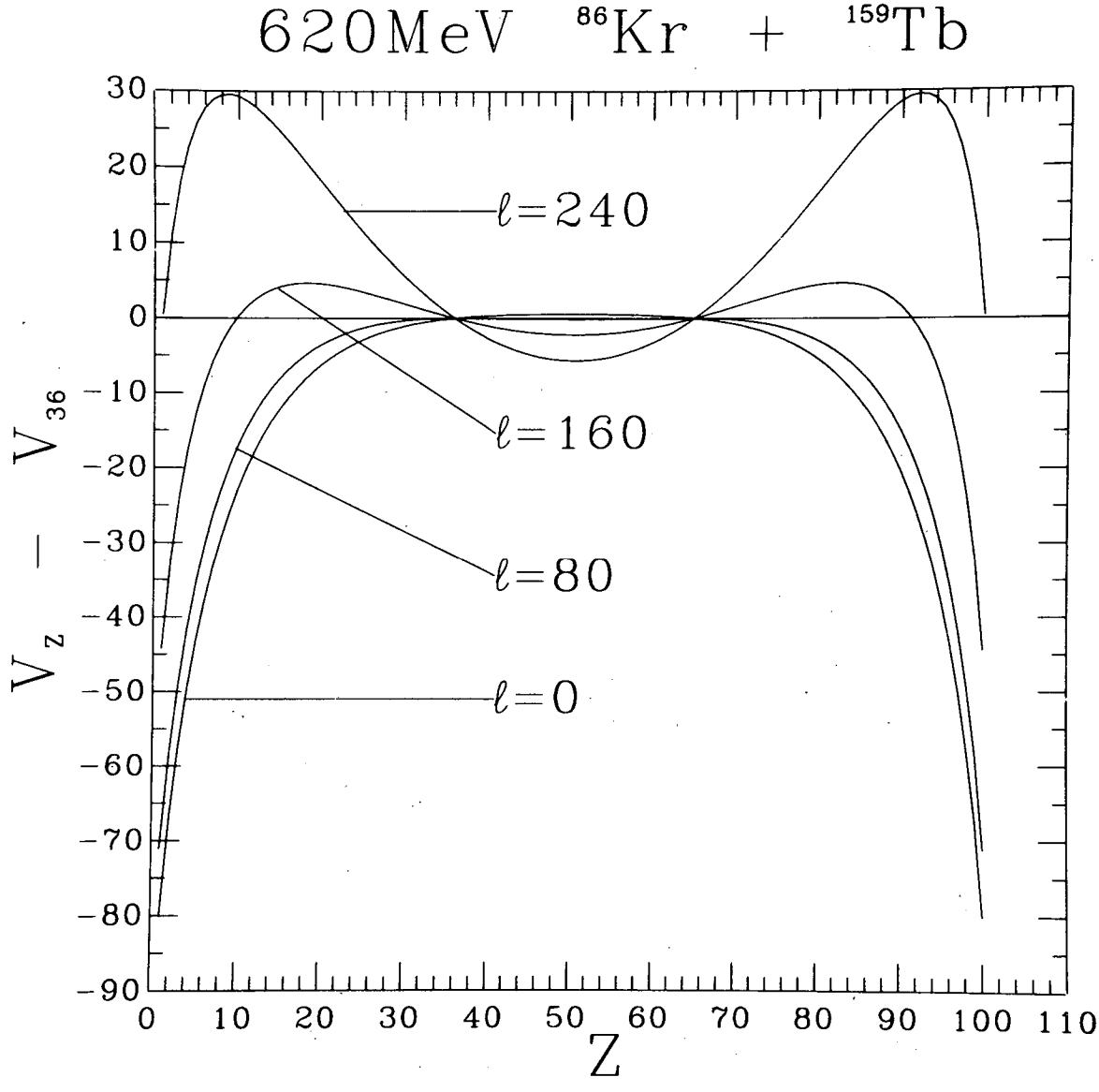

XBL 775-8597

Fig. 7

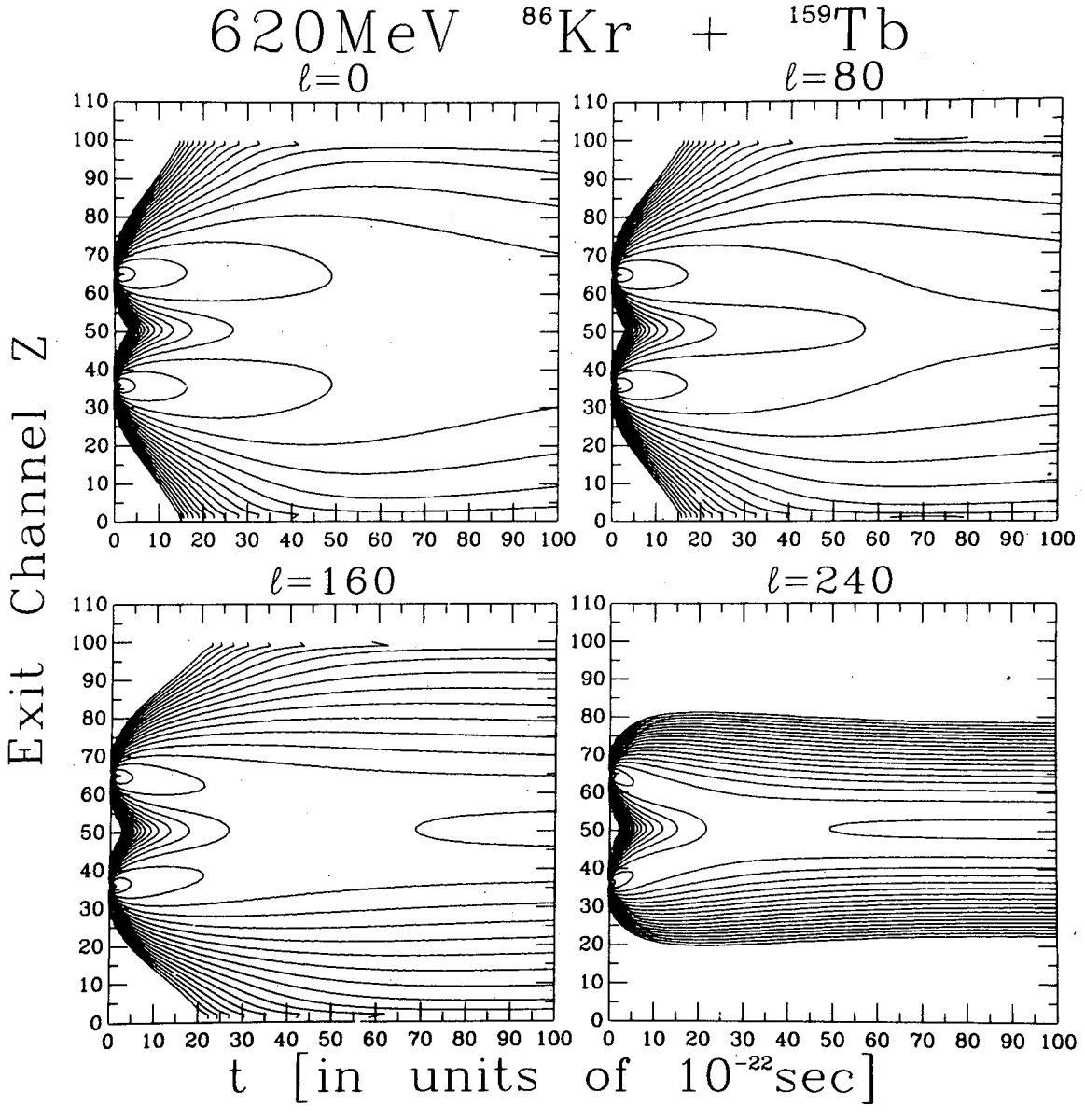

XBL 775-8599

Fig. 8

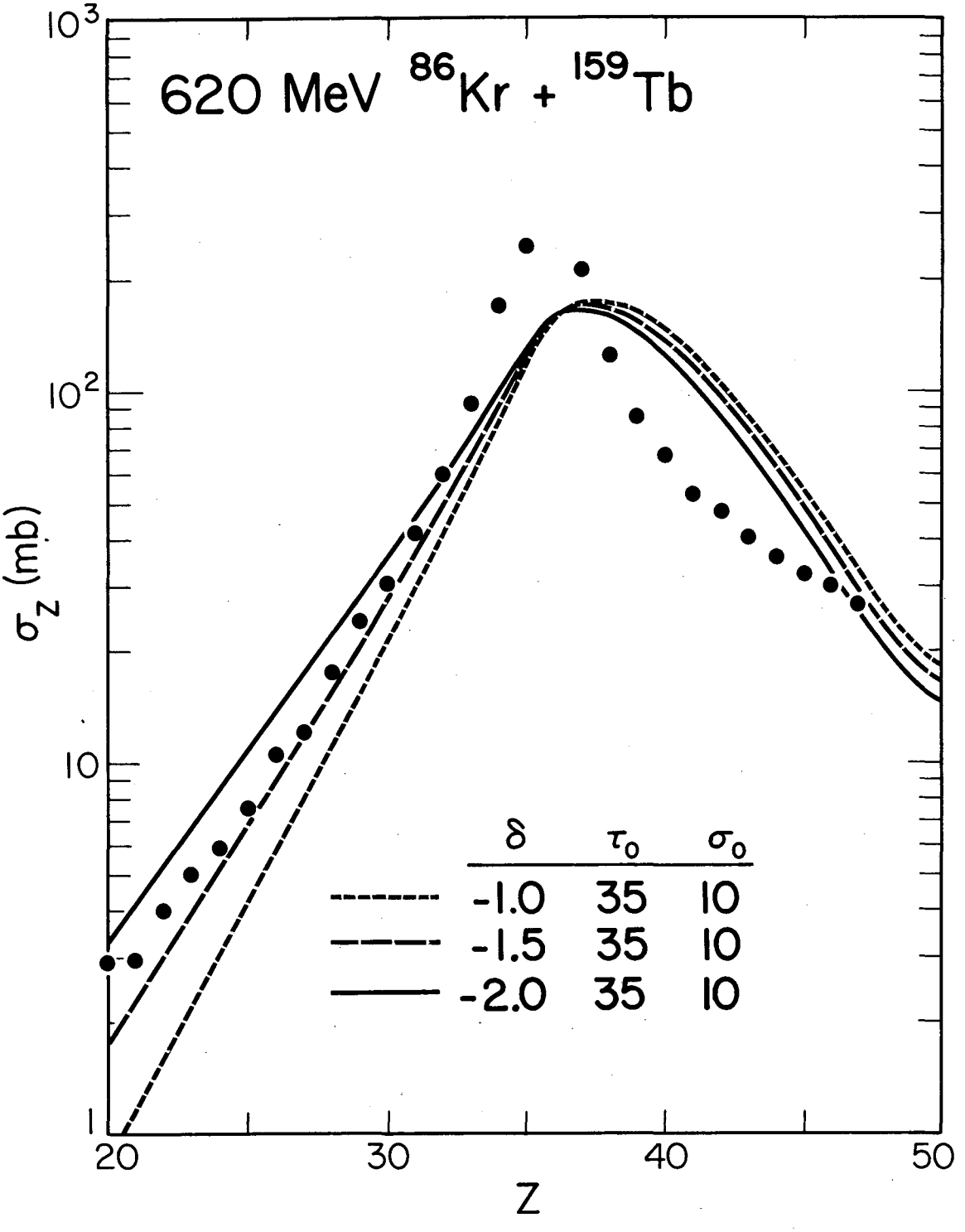

Fig. 9

XBL 777-1274

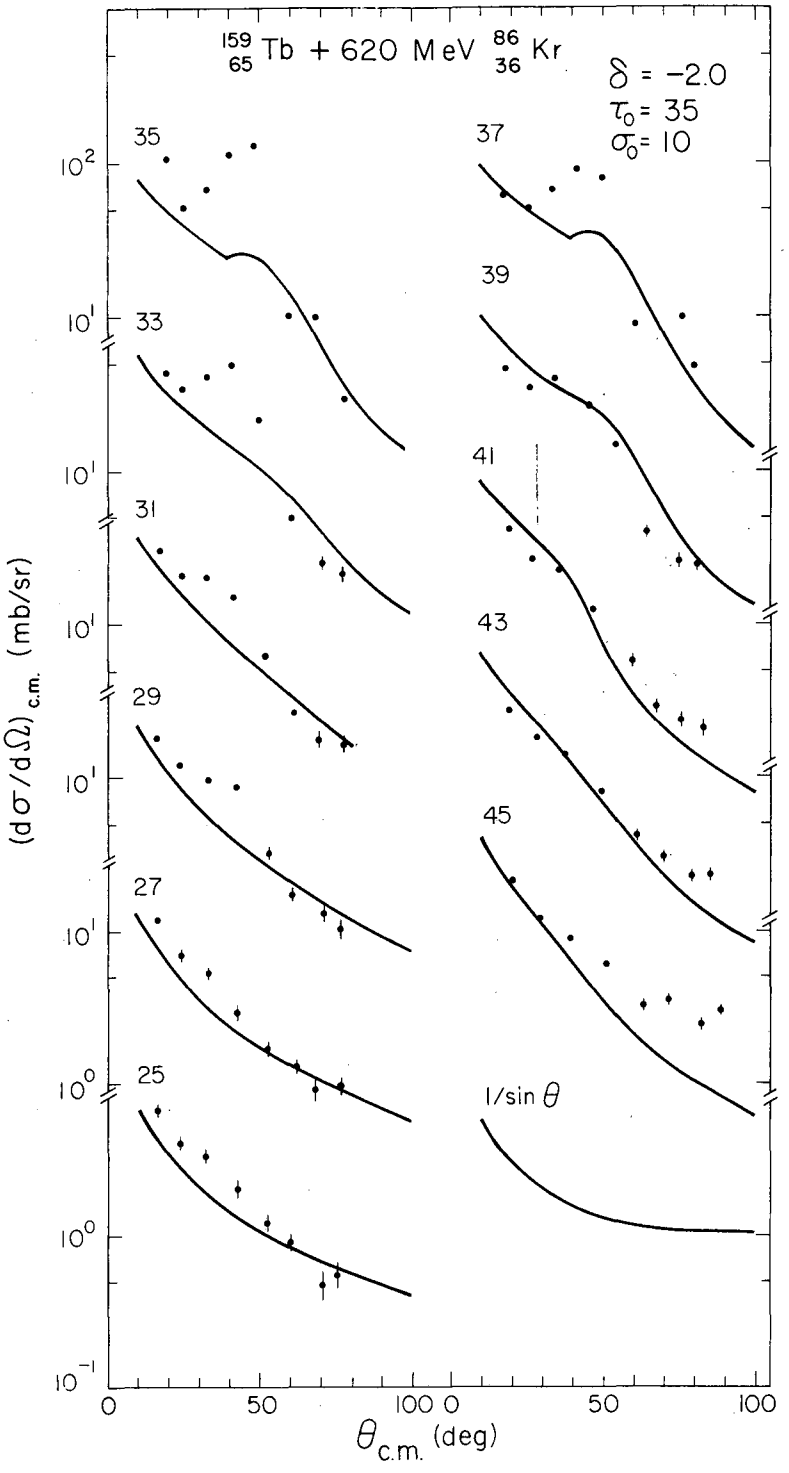

Fig. 10

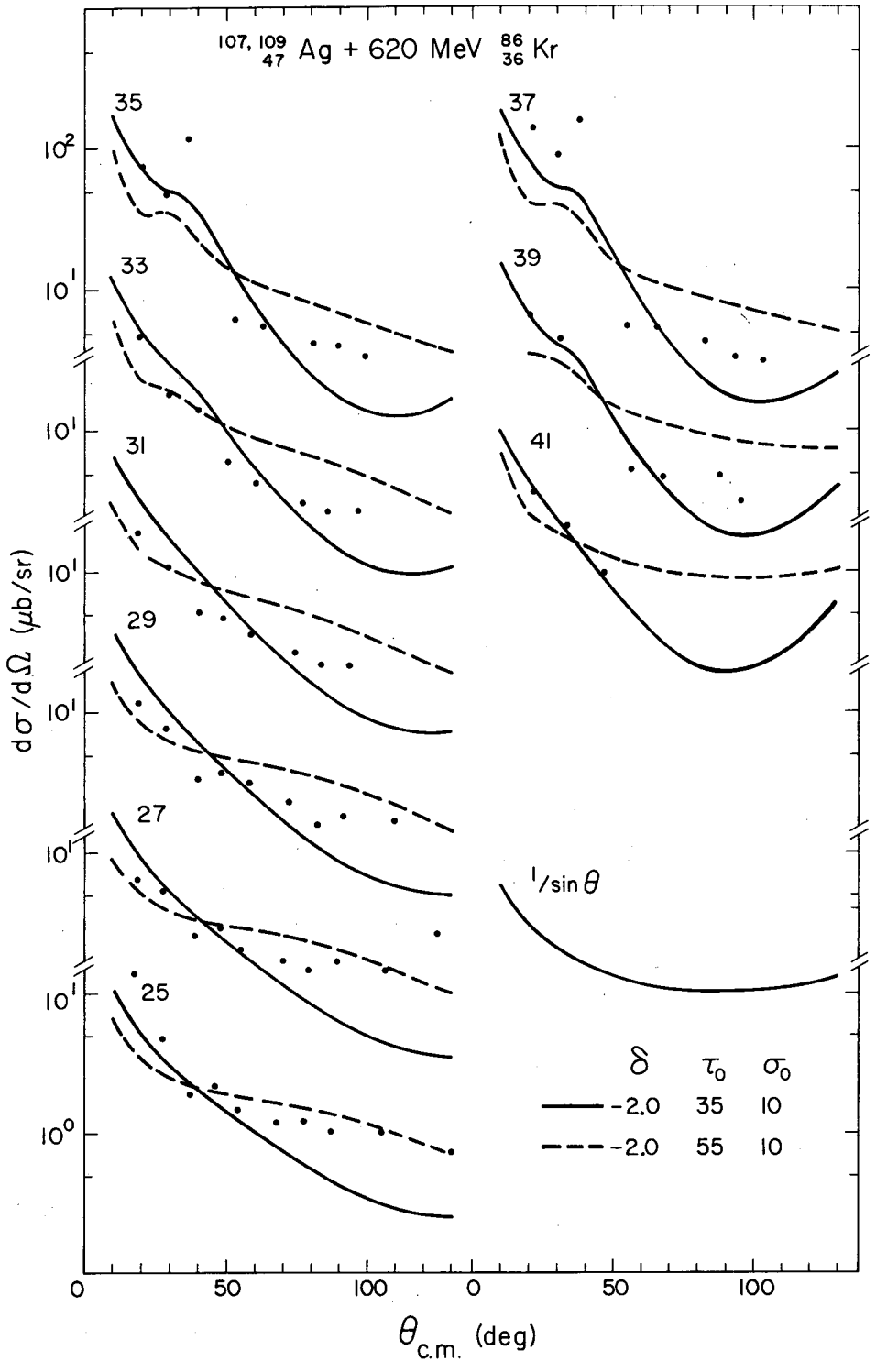

XBL 777-1276

Fig. 11

TECHNICAL INFORMATION DIVISION
LAWRENCE BERKELEY LABORATORY
UNIVERSITY OF CALIFORNIA
BERKELEY, CALIFORNIA 94720